

CHALMERS



UNIVERSITY OF GOTHENBURG

*PREPRINT 2012:16*

# Approximate global convergence in imaging of land mines from backscattered data

LARISA BEILINA  
MICHAEL V. KLIBANOV

*Department of Mathematical Sciences*  
*Division of Mathematics*  
CHALMERS UNIVERSITY OF TECHNOLOGY  
UNIVERSITY OF GOTHENBURG  
Gothenburg Sweden 2012



Preprint 2012:16

**Approximate global convergence in imaging of land  
mines from backscattered data**

Larisa Beilina and Michael V. Klibanov

Department of Mathematical Sciences  
Division of Mathematics  
Chalmers University of Technology and University of Gothenburg  
SE-412 96 Gothenburg, Sweden  
Gothenburg, September 2012

Preprint 2012:16  
ISSN 1652-9715

---

Matematiska vetenskaper  
Göteborg 2012

# Approximate global convergence in imaging of land mines from backscattered data

Larisa Beilina<sup>\*</sup> and Michael V. Klibanov<sup>†</sup>

We present new model of an approximate globally convergent method in the most challenging case of the backscattered data. In this case data for the coefficient inverse problem are given only at the backscattered side of the medium which should be reconstructed. We demonstrate efficiency and robustness of the proposed technique on the numerical solution of the coefficient inverse problem in two dimensions with the time-dependent backscattered data. Goal of our tests is to reconstruct dielectrics in land mines which is the special case of interest in military applications. Our tests show that refractive indices and locations of dielectric abnormalities are accurately imaged.

## 1 Introduction

In this paper we present the new model of the recently developed approximate globally convergent method applied [4] for the solution of the hyperbolic Multidimensional Coefficient Inverse Problem (MCIP) with backscattered data. This new model consists on the new treatment and computation of the so-called tail function which includes in the integral-differential equation of the approximate globally convergent method. Our numerical tests show efficiency of the new technique on the reconstruction of land mines from backscattered data in two dimensions.

We define a MCIP as a problem of the reconstruction of one or many unknown coefficients of a PDE distributed in space from a boundary measurements. We consider the problems only with a single measurement data, or such problems which

---

<sup>\*</sup> Department of Mathematical Sciences, Chalmers University of Technology and Gothenburg University, SE-42196 Gothenburg, Sweden, (larisa@chalmers.se)

<sup>†</sup> Department of Mathematics and Statistics University of North Carolina at Charlotte, Charlotte, NC 28223, USA, (mklibanv@uncc.edu)

use a single source location or a single direction of the propagation of incident plane wave to generate the data at the boundary.

Approximate globally convergent method of the first generation is called convexification algorithm. This method was developed in [17, 18, 28] and references therein. Approximate globally convergent method of the second generation is a different approach for solution of MCIP. This method uses layer stripping procedure with respect to the pseudo-frequency for solution of MCIPs. This approach was developed in [3, 4, 5, 6, 7, 8, 21, 22, 20] with the first publication [4] on this method.

It is well known that MCIPs are both nonlinear and ill-posed and it is very difficult answer to the question: how to obtain unknown coefficient of interest in the small neighborhood of the exact solution without a priori knowledge of any information about this solution? Approximate globally convergent method which is experimentally verified in recent works [8, 19] answers to this question. We can mention also a number of efficient one-dimensional algorithms which do not require a good first approximation, see [12, 13] and references therein. Numerically verified global reconstruction algorithms for solution of CIP with the data resulted from multiple measurements are presented in [1, 11, 15, 23, 24] and references therein. We also refer to [2] and references cited there for another method to imaging of small inclusions.

However, the case of MCIPs is more challenging one. Based on our recent numerical experience we can conclude that approximate globally convergent method is numerically efficient and can be applied in real-life reconstruction resulted from a single measurement data.

In our numerical experiments of this paper we concentrate on imaging of plastic land mines inside slowly changing background medium from backscattered data. We are not interested in imaging of slowly changing backgrounds and we do not use *a priori* knowledge of the background medium. Our examples show that we can reconstruct both locations of land mines and maximal values of the unknown coefficient inside of them in two dimensions.

## **2 Statements of Forward and Inverse Problems with backscattered data**

In this section we briefly outline an approximately globally convergent method for an MCIP for a hyperbolic PDE. For complete definition of approximate global convergence we refer to Chapter 1 of [9]. In solution of our MCIP we use single measured backscattered data. This means that we will consider hyperbolic MCIP when the wave field is initialized by the single source location or a single direction of propagation of a plane wave.

## 2.1 Statements of forward and inverse problems

We consider the following Cauchy problem as the forward problem

$$\varepsilon_r(x)u_{tt} = \Delta u, \text{ in } \mathbb{R}^n \times (0, \infty), n = 2, 3, \quad (1)$$

$$u(x, 0) = 0, u_t(x, 0) = \delta(x - x_0). \quad (2)$$

In the 2D case this equation can be derived from Maxwell's equations, see [14].

Let us define

$$n(x) = \frac{c_0}{c(x)} = \sqrt{\varepsilon_r(x)}, \quad (3)$$

where  $n(x), x \in \mathbb{R}^n, n = 2, 3$  is the spatially distributed refractive index of the medium,  $c_0$  is the speed of light in the vacuum and  $c(x)$  is the speed of propagation of the electro-magnetic field in the medium.

Let  $\Omega \subset \mathbb{R}^n, n = 2, 3$  be a convex bounded domain with the boundary  $\partial\Omega \in C^n, n = 2, 3$ . Let the coefficient  $\varepsilon_r(x)$  of equation (1) belongs to the set of admissible parameters  $M_{\varepsilon_r}$  such that

$$M_{\varepsilon_r} = \{\varepsilon_r(x) : \varepsilon_r(x) \in [1, d], \varepsilon_r(x) = 1 \forall x \in \mathbb{R}^n \setminus \Omega, \varepsilon_r(x) \in C^2(\mathbb{R}^n), n = 2, 3.\} \quad (4)$$

Here,  $d > 1$  is a given number which represents the upper boundary of the function  $\varepsilon_r(x)$ .

In the case of the *backscattered* data the data are given only at a part of the boundary of the computational domain. We will specify our computational domain  $\Omega$  with the backscattered boundary  $\Gamma$ :

$$\begin{aligned} \Omega &\subset \{x = (x_1, x_2, x_3) : x_3 > 0\}, \\ \Gamma &= \partial\Omega \cap \{x_3 = 0\} \neq \emptyset. \end{aligned}$$

In our computations we will consider cases when the wave field is originated by either the point source  $x_0 \in \{x_3 < 0\}$  at  $\{t = 0\}$  or by the incident plane wave propagating along the positive direction of the  $x_3$ -axis in the half space  $\{x_3 < 0\}$  and "falling" on the half space  $\{x_3 > 0\}$ . Thus, in the case of the backscattered data we assume that the following function  $g_0(x, t)$  is known,

$$u(x, t) = g_0(x, t), \forall (x, t) \in \Gamma \times (0, \infty). \quad (5)$$

Some of our numerical simulations of section 3 show that setting  $u := 0$  at  $\partial\Omega \setminus \Gamma$  does not affect the quality of reconstruction. Hence, we set

$$u(x, t) := g_1(x, t) = \begin{cases} g_0(x, t), & (x, t) \in \Gamma \times (0, \infty), \\ 0, & (x, t) \in (\partial\Omega \setminus \Gamma) \times (0, \infty) \end{cases} \quad (6)$$

and consider following Inverse problem:

**Inverse Problem with backscattered data (IPB1).** *Let both the domain  $\Omega$  and a part of its boundary  $\Gamma \subset \partial\Omega$  satisfy the above conditions. Suppose that the coeffi-*

cient  $\varepsilon_r(x)$  satisfies (4) and it is unknown in the domain  $\Omega$ . Determine the function  $\varepsilon_r(x)$  for  $x \in \Omega$ , assuming that the function  $g_1(x, t)$  in (6) is known for a single source position  $x_0 \in \{x_3 < 0\}$ .

Another set of our numerical simulations of section 3 we perform with the function  $u(x, t) = r_0(x, t)$  at  $\partial\Omega \setminus \Gamma$  such that this function satisfies to the following Cauchy problem

$$\begin{aligned} u_{tt} - \Delta u &= 0, \quad \text{in } \Omega \times (0, \infty), \\ u(x, 0) &= 0, \quad u_t(x, 0) = f(x), \quad \text{in } \Omega. \end{aligned} \quad (7)$$

Hence, in these tests we set

$$u(x, t) := g_2(x, t) = \begin{cases} g_0(x, t), & (x, t) \in \Gamma \times (0, \infty), \\ r_0(x, t) \in (\partial\Omega \setminus \Gamma) \times (0, \infty) \end{cases} \quad (8)$$

and consider following Inverse problem:

**Inverse Problem with backscattered data (IPB2).** Let both the domain  $\Omega$  and a part of its boundary  $\Gamma \subset \partial\Omega$  satisfy the above conditions. Suppose that the coefficient  $\varepsilon_r(x)$  satisfies (4) and it is unknown in the domain  $\Omega$ . Determine the function  $\varepsilon_r(x)$  for  $x \in \Omega$ , assuming that the function  $g_2(x, t)$  in (8) is known for a single source position  $x_0 \in \{x_3 < 0\}$ .

**Remarks 2.1.1:**

1. In the case when we initialize a plane wave instead of considering the delta-function in (2) the formulation of IPB1 or IPB2 is similar. We need only replace words “for a single source position  $x_0 \in \{x_3 < 0\}$ ” with “for a single direction of the incident plane wave propagating along the positive direction of  $x_3$ -axis in the half space  $\{x_3 < 0\}$  and falling on the half space  $\{x_3 > 0\}$ ”.

2. The question of uniqueness of IPB1 or IPB2 is an open problem. This problem can be solved via the method of Carleman estimates [16] in the case of replacing of delta-function in (2) with its approximation. Hence, if we will replace in (2) the function  $\delta(x - x_0)$  with its approximation

$$\delta_\varepsilon(x - x_0) = \frac{1}{(2\sqrt{\pi\varepsilon})^3} \exp\left(-\frac{|x - x_0|^2}{\varepsilon^2}\right)$$

for a sufficiently small  $\varepsilon > 0$ , then uniqueness will take place from results of [16]. In our considerations we assume that uniqueness holds because of applications.

## 2.2 The approximately globally convergent method

To obtain the approximately globally convergent method we start with considering the Laplace transform of the functions  $u$ ,

$$w(x, s) = \int_0^{\infty} u(x, t) e^{-st} dt, \text{ for } s > \underline{s} = \text{const.} > 0, \quad (9)$$

where  $\underline{s}$  is a sufficiently large number. We call the parameter  $s$  *pseudo frequency* and choose it experimentally, see section 3 for details. Applying Laplace transform to (1), (2) we get

$$\begin{aligned} \Delta w - s^2 \varepsilon_r(x) w &= -\delta(x - x_0), \\ \lim_{|x| \rightarrow \infty} w(x, s) &= 0. \end{aligned} \quad (10)$$

The condition  $\lim_{|x| \rightarrow \infty} w(x, s) = 0$  was established in [9, 6] for such  $\underline{s}$  that  $s > \underline{s}$ .

Let us define by  $C^{k+\alpha}$ ,  $\alpha \in (0, 1)$ ,  $k \geq 0$ , Hölder spaces. In Theorem 2.7.2 of [6] was proven that for every  $s > 0$  there exists unique solution

$$w \in C^{2+\alpha}(\mathbb{R}^3 \setminus \{|x - x_0| < \theta\}), \forall \theta > 0, \forall \alpha \in (0, 1)$$

which solves the problem (10) with  $\varepsilon(x) = 1$ , and

$$\frac{\exp(-s\sqrt{d}|x - x_0|)}{4\pi|x - x_0|} < w(x, s) \leq \frac{\exp(-s|x - x_0|)}{4\pi|x - x_0|}. \quad (11)$$

On the next step in derivation of an approximate globally convergent method we eliminate the unknown coefficient  $\varepsilon_r(x)$  from equation (10). To do that first we introduce the new function  $v(x, s)$ ,

$$v(x, s) = \frac{\ln w}{s^2}. \quad (12)$$

We are able to do that since by (11)  $w(x, s) > 0$ . We also verified this fact numerically, see Chapter 3 of [9]. Then

$$\Delta v + s^2 |\nabla v|^2 = \varepsilon_r(x), \quad x \in \Omega, \quad (13)$$

$$v|_{\partial\Omega} = \varphi(x, s), \quad \forall s \in [\underline{s}, \bar{s}], \quad (14)$$

where the function  $\varphi(x, s)$  is generated by the function  $g_1(x, t)$  in (6) or by  $g_2(x, t)$  in (8).

Now we differentiate both sides of (13) with respect to  $s$  and eliminate the coefficient  $\varepsilon_r(x)$  from (13). Denote

$$q(x, s) = \partial_s v(x, s).$$

To perform next step we need the asymptotic behavior of the function  $w(x, s)$  at  $s \rightarrow \infty$  which is confirmed by the following lemma

**Lemma 2.2.** [18]. *Assume that conditions (4) are satisfied. Let the function  $w(x, s) \in C^3(\mathbb{R}^3 \setminus \{|x - x_0| < \varepsilon\})$ ,  $\forall \varepsilon > 0$  be the solution of the problem (10). As-*

sume that geodesic lines, generated by the eikonal equation corresponding to the function  $c(x)$  are regular, i.e. any two points in  $\mathbb{R}^3$  can be connected by a single geodesic line. Let  $l(x, x_0)$  be the length of the geodesic line connecting points  $x$  and  $x_0$ . Then the following asymptotic behavior of the function  $w$  and its derivatives takes place for  $|\beta| \leq 3, k = 0, 1, x \neq x_0$

$$D_x^\beta D_s^k w(x, s) = D_x^\beta D_s^k \left\{ \frac{\exp[-sl(x, x_0)]}{f(x, x_0)} \left[ 1 + O\left(\frac{1}{s}\right) \right] \right\}, s \rightarrow \infty, \quad (15)$$

where  $f(x, x_0)$  is a certain function and  $f(x, x_0) \neq 0$  for  $x \neq x_0$ . This behavior is uniform for  $x \in \overline{\Omega}$ .

Thus, by (15) we can get the following asymptotic behavior for functions  $v(x, s)$  and  $q(x, s)$ .

$$\|v\|_{C^{2+\alpha}(\overline{\Omega})} = O\left(\frac{1}{s}\right), \|q\|_{C^{2+\alpha}(\overline{\Omega})} = O\left(\frac{1}{s^2}\right), s \rightarrow \infty. \quad (16)$$

We verify the asymptotic behavior (16) numerically in our computations, see subsection 7.2 of [9] and section 3.1.2 in [6].

Assuming that (16) holds, we obtain

$$v(x, s) = - \int_s^\infty q(x, \tau) d\tau. \quad (17)$$

We can rewrite the integral in (17) as

$$v(x, s) = - \int_s^{\bar{s}} q(x, \tau) d\tau + V(x, \bar{s}), \quad (18)$$

where the truncation number  $\bar{s} > \underline{s}$  is a large parameter which should be chosen in numerical experiments, and the function  $V(x, \bar{s})$  is defined as

$$V(x, \bar{s}) = - \int_{\bar{s}}^\infty q(x, \tau) d\tau$$

and called “the tail function”.

Using (12), we obtain an equivalent formula for the tail,

$$V(x, \bar{s}) = \frac{\ln w(x, \bar{s})}{\bar{s}^2}. \quad (19)$$

Using (12), (13) and (17) we obtain the following nonlinear integral differential equation

$$\begin{aligned}
\Delta q - 2s^2 \nabla q \cdot \int_s^{\bar{s}} \nabla q(x, \tau) d\tau + 2s \left[ \int_s^{\bar{s}} \nabla q(x, \tau) d\tau \right]^2 + 2s^2 \nabla q \nabla V \\
- 2s \nabla V \cdot \int_s^{\bar{s}} \nabla q(x, \tau) d\tau + 2s (\nabla V)^2 = 0, \quad x \in \Omega, s \in [\underline{s}, \bar{s}], \\
q|_{\partial\Omega} = \psi(x, s) := \partial_s \varphi(x, s).
\end{aligned} \tag{20}$$

From (20) we observe that the  $s$ -integrals as well as the tail function leads to the nonlinearity. By using asymptotic (16) we have that

$$\|V(x, \bar{s})\|_{C^{2+\alpha}(\bar{\Omega})} = O\left(\frac{1}{\bar{s}}\right), \bar{s} \rightarrow \infty, \tag{21}$$

From (21) follows that the tail function  $V(x, \bar{s})$  is small for large values of the truncation of pseudo frequency  $\bar{s}$ . Because of that in our first studies about approximately globally convergent method initial tail was neglected [4, 5, 6]. However, last numerical experiments have shown that our reconstruction results have a better quality if we will not neglect the initial value of the tail function rather compute it using the new model of the tail presented in the next section.

### 2.3 New model of the tail function

In this subsection we formulate our approximate mathematical model which is based on the new representation model of the tail function. We refer to section 2.9 of the book [9] for some details which we omit in the presentation below.

Let the function  $\varepsilon_r^*(x)$  satisfying (4) be the exact solution of IPB1 or IPB2 for the exact data  $g^*$  in (6). Let  $V^*(x, \bar{s})$  be the exact function for  $V$  in (19) defined as

$$V^*(x, \bar{s}) = \frac{\ln w^*(x, \bar{s})}{\bar{s}^2}. \tag{22}$$

Let  $q^*(x, s)$  and  $\psi^*(x, s)$  be the corresponding exact functions for  $q$  and  $\psi$  in (20), respectively, defined from the following nonlinear integral differential equation

$$\begin{aligned}
\Delta q^* - 2s^2 \nabla q^* \cdot \int_s^{\bar{s}} \nabla q^*(x, \tau) d\tau + 2s \left[ \int_s^{\bar{s}} \nabla q^*(x, \tau) d\tau \right]^2 + 2s^2 \nabla q^* \nabla V^* \\
- 2s \nabla V^* \cdot \int_s^{\bar{s}} \nabla q^*(x, \tau) d\tau + 2s (\nabla V^*)^2 = 0, \quad x \in \Omega, s \in [\underline{s}, \bar{s}], \\
q^*|_{\partial\Omega} = \psi^*(x, s) := \partial_s \varphi^*(x, s) \quad \forall (x, s) \in \partial\Omega \times [\underline{s}, \bar{s}].
\end{aligned} \tag{23}$$

$$q^*(x, s) \in C^{2+\alpha}(\overline{\Omega}) \times C^1[\underline{s}, \bar{s}]. \quad (24)$$

Now we describe main assumptions in the new model for the functions

$$V^*(x, \bar{s}), q^*(x, \bar{s}), \bar{s} \rightarrow \infty.$$

In our assumption we will take into account only the first term in the asymptotic behavior of the functions  $V^*(x, \bar{s}), q^*(x, \bar{s}), \bar{s} \rightarrow \infty$ . As an example we can refer to the geometrical optics assumption where the first term in the asymptotic behavior is also neglected.

**Assumptions for the functions**  $V^*(x, \bar{s}), q^*(x, \bar{s}), \bar{s} \rightarrow \infty$ .

1. Assume that the asymptotic behavior (21) take place.
2. Assume that the functions  $V^*$  and  $q^*$  have the following asymptotic behavior

$$\begin{aligned} V^*(x, \bar{s}) &= \frac{p^*(x)}{\bar{s}} + O\left(\frac{1}{\bar{s}^2}\right) \approx \frac{p^*(x)}{\bar{s}}, \quad \bar{s} \rightarrow \infty, \\ q^*(x, \bar{s}) &= \partial_{\bar{s}} V^*(x, \bar{s}) = -\frac{p^*(x)}{\bar{s}^2} + O\left(\frac{1}{\bar{s}^3}\right) \approx -\frac{p^*(x)}{\bar{s}^2}, \quad \bar{s} \rightarrow \infty. \end{aligned} \quad (25)$$

We assume that  $\Omega \subset \mathbb{R}^3$  is a convex bounded domain with the boundary

$$x_0 \notin \overline{\Omega}.$$

Setting in (23)  $s = \bar{s}$  we get

$$\begin{aligned} \Delta q^* + 2\bar{s}^2 \nabla q^* \nabla V^* + 2\bar{s} (\nabla V^*)^2 &= 0, \quad x \in \Omega, \\ q^*|_{\partial\Omega} &= \psi^*(x, \bar{s}) \quad \forall x \in \partial\Omega. \end{aligned} \quad (26)$$

Then, using the first terms in the asymptotic behavior (25) for the exact tail  $V^*(x, \bar{s}) = \frac{p^*(x)}{\bar{s}}$  and for the exact function  $q^*(x, \bar{s}) = -\frac{p^*(x)}{\bar{s}^2}$  we have

$$\begin{aligned} -\frac{\Delta p^*}{\bar{s}^2} - 2\bar{s}^2 \frac{\nabla p^*}{\bar{s}^2} \frac{\nabla p^*}{\bar{s}} + 2\bar{s} \frac{(\nabla p^*)^2}{\bar{s}^2} &= 0, \quad x \in \Omega, \\ q^*|_{\partial\Omega} &= \psi^*(x, \bar{s}) \quad \forall x \in \partial\Omega. \end{aligned} \quad (27)$$

we obtain the following *approximate* Dirichlet boundary value problem for the function  $p^*(x)$

$$\Delta p^* = 0 \text{ in } \Omega, \quad p^* \in C^{2+\alpha}(\overline{\Omega}), \quad (28)$$

$$p^*|_{\partial\Omega} = -\bar{s}^2 \psi^*(x, \bar{s}). \quad (29)$$

We now formulate our approximate mathematical model.

#### **Approximate Mathematical Model**

*Let Assumptions (1)-(2) take place. Then there exists a function  $p^*(x) \in C^{2+\alpha}(\overline{\Omega})$  such that the exact tail function  $V^*(x)$  has the form*

$$V^*(x, s) := \frac{p^*(x)}{s}, \quad \forall s \geq \bar{s}. \quad (30)$$

Using (19) we assume that

$$V^*(x, s) = \frac{p^*(x)}{\bar{s}} = \frac{\ln w^*(x, \bar{s})}{\bar{s}^2}. \quad (31)$$

Since  $q^*(x, s) = \partial_s V^*(x, s)$  for  $s \geq \bar{s}$ , we can get from (30)

$$q^*(x, \bar{s}) = -\frac{p^*(x)}{\bar{s}^2}. \quad (32)$$

Then we have the following formulas for the reconstruction of the coefficient  $\varepsilon_r^*(x)$

$$\begin{aligned} \varepsilon_r^*(x) &= \Delta v^* + s^2 |\nabla v^*|^2, \\ v^* &= -\int_s^{\bar{s}} q^*(x, \tau) d\tau + \frac{p^*(x)}{\bar{s}}. \end{aligned}$$

Now we will formulate uniqueness result for the new approximate mathematical model. Recall (20) with assumption that

$$\psi(x, \bar{s}) \in C^{2+\alpha}(\overline{\Omega}). \quad (33)$$

Consider the solution  $p(x)$  of the following boundary value problem

$$\Delta p = 0 \text{ in } \Omega, \quad p \in C^{2+\alpha}(\overline{\Omega}), \quad (34)$$

$$p|_{\partial\Omega} = -\bar{s}^2 \psi(x, \bar{s}). \quad (35)$$

There exists unique solution  $p$  of the problem (34), (35). Furthermore, it follows from (28), (29), (33), (34) and (35) that

$$\|p - p^*\|_{C^{2+\alpha}(\overline{\Omega})} \leq D\bar{s}^2 \|\psi(x, \bar{s}) - \psi^*(x, \bar{s})\|_{C^{2+\alpha}(\partial\Omega)}, \quad (36)$$

where  $D = D(\Omega) = \text{const.} > 1$ .

Now in our approximate globally convergent algorithm we take the function

$$V_{1,1}(x) := \frac{p(x)}{\bar{s}}. \quad (37)$$

as the first guess for the tail function. Here,  $p(x)$  is the solution of the problem (34)-(35).

## 2.4 The sequence of equations with respect to the pseudo-frequency

In this section from the equation (20) we will get the sequence of equations with respect to the pseudo-frequency  $s$ . For all details of this derivation we refer to [4, 9]. To do that we consider a layer stripping procedure with respect to the  $s$  by dividing the interval  $[\underline{s}, \bar{s}]$  into  $N$  small subintervals such that every interval has the step size  $h = s_{n-1} - s_n$  in the frequency. Here,

$$\underline{s} = s_N < s_{N-1} < \dots < s_0 = \bar{s}. \quad (38)$$

Now we approximate the function  $q(x, s)$  as a piecewise constant function with respect to  $s$ ,  $q(x, s) = q_n(x)$  for  $s \in [s_n, s_{n-1})$ . Using (17) and (18) the approximate value of the function  $v(x, s_n)$  is

$$v(x, s_n) = -h \sum_{j=0}^n q_j(x) + V(x, \bar{s}), q_0(x) \equiv 0. \quad (39)$$

We now describe the procedure how obtain a sequence of approximate Dirichlet boundary value problems for elliptic PDEs for functions  $q_n(x)$ . Let us introduce the  $s$ -dependent Carleman Weight Function (CWF)

$$\mathcal{C}_{n,\mu}(s) = \exp[\mu(s - s_{n-1})], \quad (40)$$

where  $\mu > 1$  is a large parameter, which is chosen in numerical experiments. Multiplying both sides of equation (20) by  $\mathcal{C}_{n,\mu}(s)$  and integrating over  $(s_n, s_{n-1})$ , we obtain following system of equations with respect to the pseudo-frequency for  $x \in \Omega$

$$\begin{aligned} L_n(q_n) &:= \Delta q_n - A_{1,n} \left( h \sum_{j=0}^{n-1} \nabla q_j - \nabla V_n \right) \nabla q_n \\ &= B_n (\nabla q_n)^2 - A_{2,n} h^2 \left( \sum_{j=0}^{n-1} \nabla q_j \right)^2 \\ &\quad + 2A_{2,n} \nabla V_n \left( h \sum_{j=0}^{n-1} \nabla q_j \right) - A_{2,n} (\nabla V_n)^2, \\ q_n \mid_{\partial\Omega} &= \psi_n(x) := \frac{1}{h} \int_{s_n}^{s_{n-1}} \psi(x, s) ds, \quad n = 1, \dots, N. \end{aligned} \quad (41)$$

Here numbers  $A_{1,n}, A_{2,n}, B_n := \frac{I_{1,n}}{I_0}$  depends on  $\mu, h, n$  can be computed explicitly via formulas

$$\begin{aligned}
I_0 &:= I_0(\mu, h) = \int_{s_n}^{s_{n-1}} \mathcal{C}_{n,\mu}(s) ds, \\
I_{1,n} &:= I_{1,n}(\mu, h) = \int_{s_n}^{s_{n-1}} s(s_{n-1} - s)[s - (s_{n-1} - s)] \mathcal{C}_{n,\mu}(s) ds, \\
A_{1,n} &:= A_{1,n}(\mu, h) = \frac{2}{I_0} \int_{s_n}^{s_{n-1}} s[s - 2(s_{n-1} - s)] \mathcal{C}_{n,\mu}(s) ds, \\
A_{2,n} &:= A_{2,n}(\mu, h) = \frac{2}{I_0} \int_{s_n}^{s_{n-1}} s \mathcal{C}_{n,\mu}(s) ds.
\end{aligned} \tag{42}$$

In (41) functions  $V_n$  are determined from the iterative procedure described in the next section. Because of the presence of the CWF in (41) we observe that  $\lim_{\mu \rightarrow \infty} B_n = 0$  uniformly for all  $n$  with  $\mu \gg 1$ . We describe details of numerical determining of this parameter in Chapter 3 of [9].

In system (41) we have two unknown functions,  $q_n$  and  $V_n$ . We solve system (41) iteratively on every pseudo-frequency interval. First, we compute  $V_n$  by iterative procedure inside every pseudo-frequency interval, and then by knowing  $V_n$  we determine the function  $q_n$  by solving the equation (41). Details of the iterative procedure are described in the next section.

## 2.5 The Approximate Globally Convergent Algorithm

We present now algorithm for the numerical solution of equations (41). In this algorithm index  $k$  denotes the number of iterations inside every pseudo-frequency interval.

Step 0 Iteration  $(n, 1), n \geq 1$ . On this step we describe iterations with respect to the nonlinear term  $(\nabla q_n)^2$  in (41). Suppose that the initial tail function  $V_{n,0}(x, \bar{s}) \in C^{2+\alpha}(\bar{\Omega})$  is determined from (37). Suppose also that functions  $q_{1,1}^0, \dots, q_{n,1}^0 \in C^{2+\alpha}(\bar{\Omega})$  are already constructed. Then, we solve iteratively with respect to the nonlinear term the following Dirichlet boundary value problems, for  $k = 1, 2, \dots$

$$\begin{aligned}
\Delta q_{n,1}^k - A_{1n} \left( h \sum_{j=1}^{n-1} \nabla q_j \right) \cdot \nabla q_{n,1}^k + A_{1n} \nabla q_{n,1}^k \cdot \nabla V_{n,0} \\
= 2B_{1,n} \left( \nabla q_{n,1}^{k-1} \right)^2 - A_{2n} h^2 \left( \sum_{j=1}^{n-1} \nabla q_j(x) \right)^2 \\
+ 2A_{2n} \nabla V_{n,0} \cdot \left( h \sum_{j=1}^{n-1} \nabla q_j(x) \right) - A_{2n} (\nabla V_{n,0})^2, \\
q_{n,1}^k = \bar{\psi}_n(x), \quad x \in \partial\Omega.
\end{aligned}$$

We obtain the function  $q_{n,1} := \lim_{k \rightarrow \infty} q_{n,1}^k$  such that  $q_{n,1} \in C^{2+\alpha}(\bar{\Omega})$ .

Step 1 Compute  $\varepsilon_{r_{n,1}}$  via backwards calculations using the finite element formulation of the equation (10), see details in Chapter 3 of [9], or via the finite difference discretization of (39)

$$\varepsilon_{r_{n,1}}(x) = \Delta v_{n,1} + s_n^2 |v_{n,1}|^2, x \in \Omega,$$

where functions  $v_{n,1}$  are defined as

$$v_{n,1}(x) = -hq_{n,1} - h \sum_{j=0}^{n-1} q_j + V_{n,1}(x).$$

Step 2 Solve the hyperbolic forward problem (1)-(2) with  $\varepsilon_{rn}(x) := \varepsilon_{r_{n,1}}(x)$ , calculate the Laplace transform and the function  $w_{n,1}(x, \bar{s})$ .

Step 3 Find a new approximation for the tail function

$$V_{n,1}(x) = \frac{\ln w_{n,1}(x, \bar{s})}{\bar{s}^2}. \quad (43)$$

Step 4 Iterations  $(n, i)$ ,  $i \geq 2, n \geq 1$ . We now iterate with respect to the tails (43).

Suppose that functions  $q_{n,i-1}, V_{n,i-1}(x, \bar{s}) \in C^{2+\alpha}(\bar{\Omega})$  are already constructed.

Step 5 Solve the boundary value problem

$$\begin{aligned} \Delta q_{n,i} - A_{1n} \left( h \sum_{j=1}^{n-1} \nabla q_j \right) \cdot \nabla q_{n,i} + A_{1n} \nabla q_{n,i} \cdot \nabla V_{n,i-1} \\ = 2B_{1,n} (\nabla q_{n,i-1})^2 - A_{2n} h^2 \left( \sum_{j=1}^{n-1} \nabla q_j(x) \right)^2 \\ + 2A_{2n} \nabla V_{n,i-1} \cdot \left( h \sum_{j=1}^{n-1} \nabla q_j(x) \right) - A_{2n} (\nabla V_{n,i-1})^2, \\ q_{n,i}(x) = \bar{\psi}_n(x), \quad x \in \partial\Omega. \end{aligned}$$

Step 6 Compute  $\varepsilon_{r_{n,i}}$  by backwards calculations using the finite element formulation of the equation (10) or via the finite difference discretization of (39)

$$\varepsilon_{r_{n,i}}(x) = \Delta v_{n,i} + s_n^2 |v_{n,i}|^2, x \in \Omega,$$

where functions  $v_{n,i}$  are defined as

$$v_{n,i}(x) = -hq_{n,i} - h \sum_{j=0}^{n-1} q_j + V_{n,i}(x).$$

We note that the function  $\varepsilon_{r_{n,i}}(x)$  is extended in  $\mathbb{R}^n \setminus \Omega, n = 2, 3$  by unity, see (4).

- Step 7 Solve the hyperbolic forward problem (1)-(2) with  $\varepsilon_{rn,i}$ , compute the Laplace transform and obtain the function  $w_{n,i}(x, \bar{s})$ .
- Step 8 Find a new approximation for the tail function

$$V_{n,i}(x) = \frac{\ln w_{n,i}(x, \bar{s})}{\bar{s}^2}.$$

- Step 9 Iterate with respect to  $i$  and stop iterations at  $i = m_n$  such that  $q_{n,m_n} := \lim_{i \rightarrow \infty} q_{n,i}^k$ . Stopping criterion for computing functions  $q_{n,i}^k$  is

$$\text{either } F_n^k \geq F_n^{k-1} \text{ or } F_n^k \leq \eta, \quad (44)$$

where  $\eta$  is a chosen tolerance and  $F_n^k$  are defined as

$$F_n^k = \frac{\|q_{n,i}^k - q_{n,i}^{k-1}\|_{L_2}}{\|q_{n,i}^{k-1}\|_{L_2}}$$

- Step 10 Set

$$q_n := q_{n,m_n}, \quad \varepsilon_{rn}(x) := \varepsilon_{rn,m_n}(x), \quad V_{n+1,0}(x) := \frac{\ln w_{n,m_n}(x, \bar{s})}{\bar{s}^2}.$$

- Step 11 We stop computing functions  $\varepsilon_{rn,i}^k$  when

$$\text{either } N_n \geq N_{n-1} \text{ or } N_n \leq \eta, \quad (45)$$

where

$$N_n = \frac{\|\varepsilon_{rn}^k - \varepsilon_{rn}^{k-1}\|_{L_2(\Omega)}}{\|\varepsilon_{rn}^{k-1}\|_{L_2(\Omega)}}. \quad (46)$$

## 2.6 Approximate Global Convergence Theorem

We now present a brief formulation of the approximate global convergence Theorem 2.9.4 of the book [9]. We refer also to Theorem 2.9.4 of [9] for the full details and proof of this theorem.

**Approximate Global Convergence Theorem** [9]. Let  $\Omega \subset \mathbb{R}^3$  be the above convex bounded domain with the boundary  $\partial\Omega \in C^3$  and the source  $x_0 \notin \overline{\Omega}$ . Let  $\Omega_1 \subset \mathbb{R}^3$  be another bounded domain and  $\Omega \subset \subset \Omega_1$ . Let the above Assumption holds. Suppose that all functions  $\psi_n \in C^{2+\alpha}(\partial\Omega)$  and functions  $\varepsilon_r^{n,k}(x) \geq 1$  in  $\overline{\Omega}$ . Also, assume that the exact solution  $\varepsilon_r^*(x)$  of IP1 satisfies condition (4) and  $\varepsilon_r^* \in C^\alpha(\overline{\Omega})$ . Suppose that the total number of inner iterations for is  $m := m_n, \forall n \in [1, N]$ . Also assume that then number of  $s$ -subintervals  $\tilde{N}$  covered by the above algorithm is independent on the step size  $h$  in the  $s$ -direction. Let  $\psi_n^* \in C^{2+\alpha}(\partial\Omega)$  be functions  $\psi_n$  corresponding to the exact solution  $\varepsilon_r^*(x)$  and

$$\|\psi_n - \psi_n^*\|_{C^{2+\alpha}(\partial\Omega)} \leq C^*(h + \sigma),$$

where  $\sigma$  is the level of the error in the boundary data  $g_1(x, t)$  in (6) or  $g_2(x, t)$  in (8) and  $C^* = \text{const.} > 1$ . Denote

$$\eta = 2(h + \sigma).$$

Let the number  $\bar{s} > 1$ . Choose the parameter  $\mu$  in the Carleman weight function (40) so large that

$$\mu > \frac{8(\bar{s}C^*)^2}{\eta}.$$

Then there exists a constant  $M = M(\bar{s}, C^*, d, \Omega, \Omega_1) > 2$  such that if the number  $\eta$  is so small that

$$\eta \in (0, \eta_0), \eta_0 = \frac{1}{\bar{N}M^{3\bar{N}m}},$$

then all functions  $\varepsilon_r^{n,k} \in C^\alpha(\bar{\Omega})$  and the following accuracy estimate of the Hölder type holds

$$\left\| \varepsilon_r^{n,k} - \varepsilon_r^* \right\|_{C^\alpha(\bar{\Omega})} \leq \eta^\omega := \varepsilon \in (0, 1), \quad (47)$$

where the number  $\omega \in (0, 1)$  is

$$\omega = \frac{\ln(\bar{N}M)}{3\bar{N}m \ln M + \ln(\bar{N}M)}.$$

Our numerical experience has shown that one can always choose a proper stopping number  $\bar{N}$  for iterations. It follows from (47) that we have Hölder-like convergence estimate.

### 3 Imaging of land mines with backscattered data

In this section we present numerical implementation of approximately globally convergent method on an example of reconstruction of land mines using backscattered data. For the case when Quasi-Reversibility Method (QRM) is used for such reconstruction we refer to results of [22, 21, 28]. In this work we use finite element discretization for solution of an integro-differential equation (41) on every pseudo-frequency interval rather than using QRM method of [22, 21, 28]. Our numerical tests show that we can get very accurate reconstruction of location and refractive indexes of objects with backscattered data without using of QRM.

In our implementation we use some discrepancies between the theory of approximate globally convergent method and the practical computations in our specific case of imaging of land mines.

1. The *first* main discrepancy is with regard to Lemma 2.2. By this lemma, we need to have regularity of geodesic lines generated by the eikonal equation [26]

$$|\nabla_x l(x, x_0)|^2 = \varepsilon_r(x), \quad (48)$$

where  $l(x, x_0)$  is the length of the geodesic line connecting points  $x$  and  $x_0$ .

The regularity condition is not constructive and cannot be verified analytically. It can be verified only in the case when  $\varepsilon_r(x)$  is close to the constant. We have verified the asymptotic behavior of Lemma 2.2 computationally, see Chapter 3 of [9].

2. The *second* main discrepancy is that we perform our computations with the plane wave instead of the point source in (2). We need the point source in (2) only because of conditions of Lemma 2.2. However, the technique of approximate globally convergence can be easily extended to the case of the plane wave. From other side, in the case of our application to image plastic land mines, the wave which is initialized by a point source, overcomes to a plane wave when that source is located far from the domain of interest.

### 3.1 A simplified Mathematical Model of Imaging of Plastic Land Mines

We use some simplification assumptions in our experiments to image plastic land mines. First, we consider the 2D case instead of 3D. Second, we ignore the air/ground interface and assume that our hyperbolic PDE (1)-(2) is valid in the whole space.

Let the ground be  $\{\mathbf{x} = (x, z) : z > 0\} \subset \mathbb{R}^2$ . Suppose that a polarized electric field is generated by a plane wave, which is initialized at the line  $\{z = z^0 < 0, x \in \mathbb{R}\}$  at the moment of time  $t = 0$ .

We use the well-known fact that the maximal depth of an antipersonnel land mine does not exceed approximately 10 centimeters (cm)=0.1 meter (m). In our test we model these mines as small rectangles with length of side 0.2 meter and width of side 0.1 meter. We are interested in imaging of land mines when one mine is lying over another one. We have modelled such situation in our computational geometry  $\Omega$ , see Figure 1. This is one of the important and practical cases of military applications. We set

$$\tilde{\Omega}_{FEM} = \{\mathbf{x} = (x, z) \in (-0.3, 0.3) \text{ m} \times (0.05, 0.45) \text{ m}\}.$$

Now we introduce dimensionless spatial variables  $\mathbf{x}' = \mathbf{x} / (0.1 \text{ m})$  and obtain that the domain  $\tilde{\Omega}_{FEM}$  is transformed into our dimensionless computational domain

$$\Omega_{FEM} = (-3.0, 3.0) \times (0.5, 4.5).$$

Using tables of dielectric constants [27] we see that in the dry sand  $\varepsilon_r = 5$  and in the trinitrotoluene (TNT)  $\varepsilon_r = 22$ . Hence, the relation of mine/background contrast

is  $22/5 \approx 4$ . Thus, we consider new parameters

$$\varepsilon_r' = \frac{\varepsilon_r}{5},$$

to get

$$\varepsilon_r(\text{dry sand}) = 1, \quad \varepsilon_r(\text{TNT}) \approx 4. \quad (49)$$

To simulate the data for the inverse problem, we solve the forward problem using the software package WavES [29] via the hybrid FEM/FDM method described in [10]. The dimensionless size of our computational domain for the forward problem is  $\Omega = [-4.0, 4.0] \times [0, 5.0]$ . This domain is split into a dimensionless finite element domain  $\Omega_{FEM} = [-3.0, 3.0] \times [0.5, 4.5]$  and a surrounding domain  $\Omega_{FDM}$  with a structured mesh,  $\Omega = \Omega_{FEM} \cup \Omega_{FDM}$ , see Figure 1. The space mesh in  $\Omega_{FEM}$  and in  $\Omega_{FDM}$  consists of triangles and squares, respectively. The mesh size is  $\tilde{h} = 0.125$  in the overlapping regions. The boundary of the domain  $\Omega$  is  $\partial\Omega = \partial\Omega_1 \cup \partial\Omega_2 \cup \partial\Omega_3$ . Here,  $\partial\Omega_1$  and  $\partial\Omega_2$  are respectively top and bottom sides of the domain  $\Omega$ , see Figure 1, and  $\partial\Omega_3$  is the union of left and right sides of this domain.

Correspondingly to the boundaries of  $\Omega_{FDM}$  we describe also boundaries of  $\Omega_{FEM}$  where we solve our inverse problem. We define the boundary of the domain  $\Omega_{FEM}$  as  $\Gamma = \Gamma_1 \cup \Gamma_2 \cup \Gamma_3$ . Here,  $\Gamma_1$  and  $\Gamma_2$  are respectively top and bottom sides of the domain  $\Omega_{FEM}$ , see Figure 1, and  $\Gamma_3$  is the union of left and right sides of this domain.

We use the hybrid method of [10] since in our applications we know value of the coefficient  $\varepsilon_r(\mathbf{x})$  outside of the domain of interest  $\Omega_{FEM}$ . That means that we know

$$\varepsilon_r(\mathbf{x}) = 1 \text{ in } \Omega_{FDM}, \quad (50)$$

and we need to determine  $\varepsilon_r(\mathbf{x})$  only in  $\Omega_{FEM}$ . Thus, it is computationally efficient consider the forward problem in the whole computational domain  $\Omega$  but solve the coefficient inverse problem only in  $\Omega_{FEM}$ . In the case of our application the hybrid method of [10] perfectly corresponds to these needs.

Now we proceed to the forward problem which is used in our computations. The forward problem in our test is

$$\begin{aligned} \varepsilon_r(\mathbf{x}) u_{tt} - \Delta u &= 0, \quad \text{in } \Omega \times (0, T), \\ u(\mathbf{x}, 0) &= 0, \quad u_t(\mathbf{x}, 0) = 0, \quad \text{in } \Omega, \\ \partial_n u &= f(t), \quad \text{on } \partial\Omega_1 \times (0, t_1], \\ \partial_n u &= -\partial_t u, \quad \text{on } \partial\Omega_1 \times (t_1, T), \\ \partial_n u &= -\partial_t u, \quad \text{on } \partial\Omega_2 \times (0, T), \\ \partial_n u &= 0, \quad \text{on } \partial\Omega_3 \times (0, T), \end{aligned} \quad (51)$$

where  $f(t)$  is the amplitude of the initialized plane wave,

$$f(t) = \frac{(\sin(\omega t - \pi/2) + 1)}{10}, \quad 0 \leq t \leq t_1 := \frac{2\pi}{\omega}. \quad (52)$$

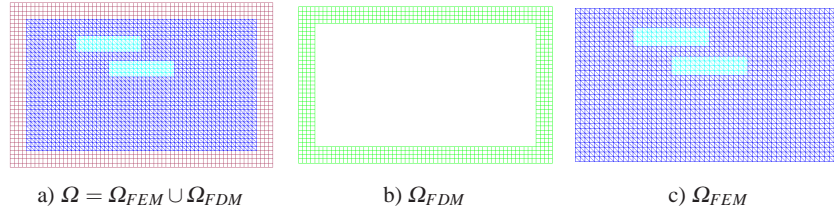


**Fig. 1** a) Geometry of the hybrid mesh. This is a combination of the quadrilateral mesh in the subdomain  $\Omega_{FDM}$  b), where we apply FDM, and the finite element mesh in the inner domain  $\Omega_{FEM}$  c), where we use FEM. The solution of the inverse problem is computed in  $\Omega_{FEM}$ . The trace of the solution of the forward problem (51) is recorded at the top boundary  $\Gamma_1$  of the finite element domain  $\Omega_{FEM}$ .

To compute the data for the inverse problem we solve the forward problem (51) with  $\omega = 7.0$  in (52) and in the time  $T = (0, 6)$  with the time step  $\tau = 0.01$  which is satisfied to the CFL condition, and save solution of this problem at the top boundary  $\Gamma_1$  of the finite element domain  $\Omega_{FEM}$ . Figures 2 show how the plane wave propagates in the computational domain  $\Omega$  presented at Figure 1-a).

Because of (49), we define the set of admissible coefficients for the function  $\varepsilon_r(\mathbf{x})$  in  $\Omega_{FEM}$  as

$$M_{\varepsilon_r} = \{ \varepsilon_r(\mathbf{x}) : \varepsilon_r(\mathbf{x}) \in [1, 8], \varepsilon_r(\mathbf{x}) = 1 \forall \mathbf{x} \in \mathbb{R}^2 \setminus \Omega, \varepsilon_r(\mathbf{x}) \in C^2(\mathbb{R}^2) \}.$$

### 3.2 Numerical Results

We have performed two set of tests. In the first test we solved IPB1 and in the second test we solved IPB2. The goal of both tests was to reconstruct structure given on Figure 1-a).

The data at the boundary  $\Gamma_1$  for IPB1 or IPB2 were computationally simulated using the software package WavES [29] via solving the hyperbolic problem (51) with known values of the coefficient  $\varepsilon_r = 4$  inside two inclusions of Figure 1-a). To choose appropriate pseudo-frequency interval for computational solution of IPB1 or IPB2 we check sensitivity of the simulated backscattered data at the boundary  $\Gamma_1$  by solution of the forward problem (51).

Thus, we check sensitivity of the simulated function  $q(\mathbf{x}, s)$  with respect to the pseudo-frequency  $s$ . Figure 4 displays the computed function  $q(\mathbf{x}, s)$ ,  $\mathbf{x} \in \Gamma_1$  for different values of the pseudo-frequency  $s$ . We have started computations of the function  $q(\mathbf{x})$  from very large values of the pseudo-frequency  $s = 18$  and finished with small values  $s = 2$ . From Figure 4 we have observed that the behavior of the function  $|q(\mathbf{x}, s)|$  for  $\mathbf{x} \in \Gamma_1$  is similar for all pseudo frequencies  $s \leq 5$ . More precisely, this function is close to its maximal value only on a small part of the backscattered side  $\Gamma_1$ , see Figure 4. However, all values of the function  $|q(\mathbf{x})|$  for  $s > 5$  are very

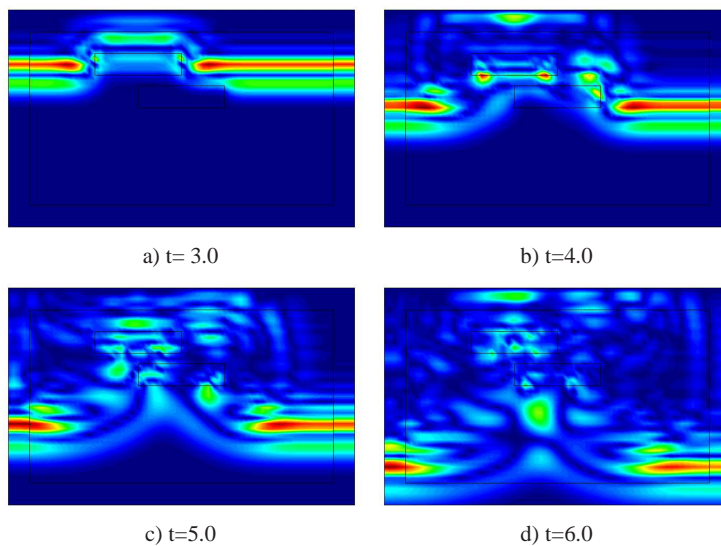


**Fig. 2** Isosurfaces of the simulated exact solution for the forward problem (51) at different times with a plane wave initialized at the top boundary.

noisy and does not show sensitivity to the inclusions, see Figure 4-e), f). Thus, for computations we decided take one of pseudo-frequency intervals for  $s < 5$ . Using Figure 4 we observe that the computed function  $q(\mathbf{x}, s)$  is most sensitive on the interval  $s = [2, 3]$  then on other intervals in the pseudo-frequency, and we take the pseudo-frequency interval  $s = [2, 3]$  for our computations. We take step in pseudo-frequency  $h = 0.05$  and run computations from  $\bar{s} = 3$  to  $\underline{s} = 2$ . We have used derivatives of tails  $\partial_{\bar{s}} V_{n,i}(\mathbf{x}, \bar{s})$  instead of tails  $V_{n,i}(\mathbf{x}, \bar{s})$  when computing functions  $q_{n,i}$ , see Chapters 2,5 of [9] for explanations. To solve integral-differential equation (41) we use Finite Element discretization of this equation with piecewise-linear functions for approximation of functions  $q_n(\mathbf{x})$  and then we use KSP method in the software package PETSc [25] for solution of the resulting equation.

### 3.3 Test1

In this test we solve IPB1. The boundary conditions for the integral-differential equation (41) were replaced with the following Dirichlet boundary conditions

$$q_n|_{\Gamma_1} = \psi_n(\mathbf{x}), \quad q_n|_{\Gamma_2 \cup \Gamma_3} = 0. \quad (53)$$

Thus, we use the zero Dirichlet boundary condition for the function  $q_n$  at  $\Gamma_2 \cup \Gamma_3$ . This condition does not follow from the radiation condition at the infinity for the

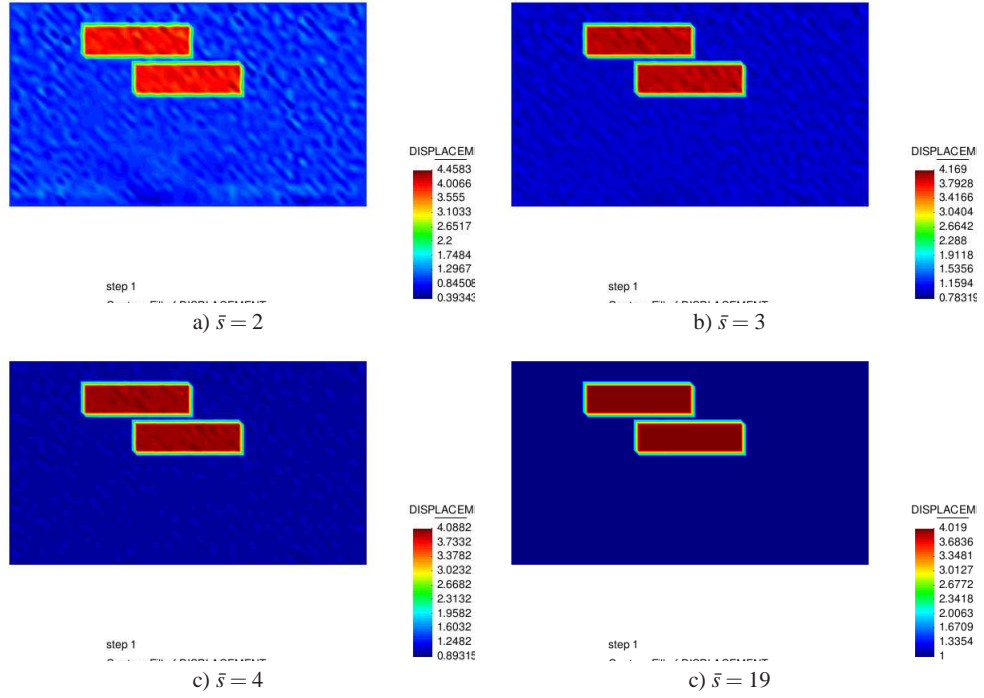


**Fig. 3** Reconstruction results in Test 1 with the computed exact tail  $V_h = \frac{\ln w_h(x, \bar{s})}{\bar{s}^2}$  at different pseudo-frequencies  $\bar{s}$ .

function  $w(\mathbf{x}, s)$ . However, we have observed in our computational simulations that values of functions  $|q_n(\mathbf{x})|$  at  $I_1$  are much larger and close to the constant than values of  $|q_n(\mathbf{x})|$  at  $\mathbf{x} \in I_2 \cup I_3$ .

The algorithm of section 2.5 was used to calculate the image of Figure 5-a). Location of both the mine-like targets is imaged accurately although we could not separate these two mines. Also,  $\varepsilon_{r,comp}(\mathbf{x}) = 1$  outside of the imaged inclusions is reconstructed correctly. Finally,  $\max[\varepsilon_{r,comp}(\mathbf{x})] \approx 3.58$  which is 89.5% of the correct value.

### 3.4 Test2

In this test we solve IPB2. The boundary conditions for the integral-differential equation (41) were replaced with the following Dirichlet boundary conditions

$$q_n|_{I_1} = \psi_{1_n}(\mathbf{x}), \quad q_n|_{I_2 \cup I_3} = \psi_{2_n}(\mathbf{x}),$$

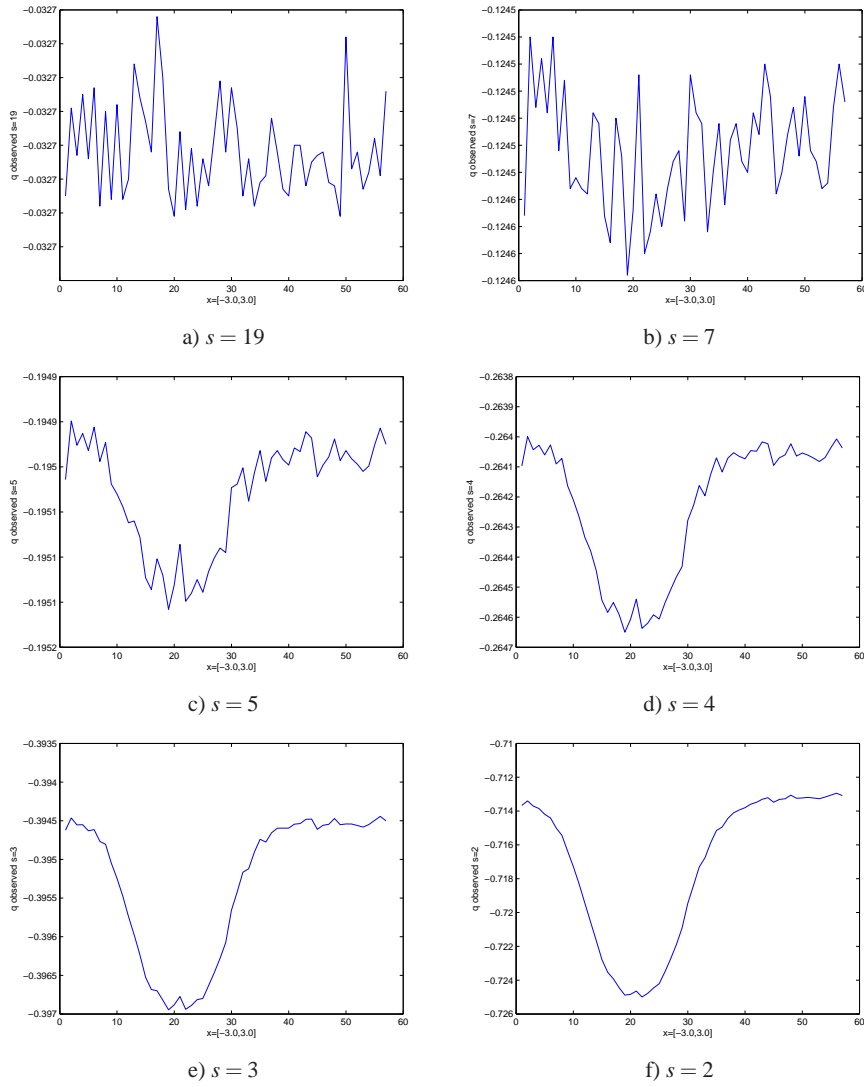


**Fig. 4** Backscattered data for the function  $q$  at the top boundary  $\Gamma_1$  of the computational domain  $\Omega_{FEM}$  computed for the different values of the pseudo-frequency  $s$ . We observe that for all pseudo-frequencies  $s \leq 5$ , the values of the function  $|q(x, s)|$  are close to its maximal value only on a small part of the boundary  $\Gamma_1$ . Values of the function  $q(x, s)$  at the rest of  $\Gamma_1$  are close to a constant.

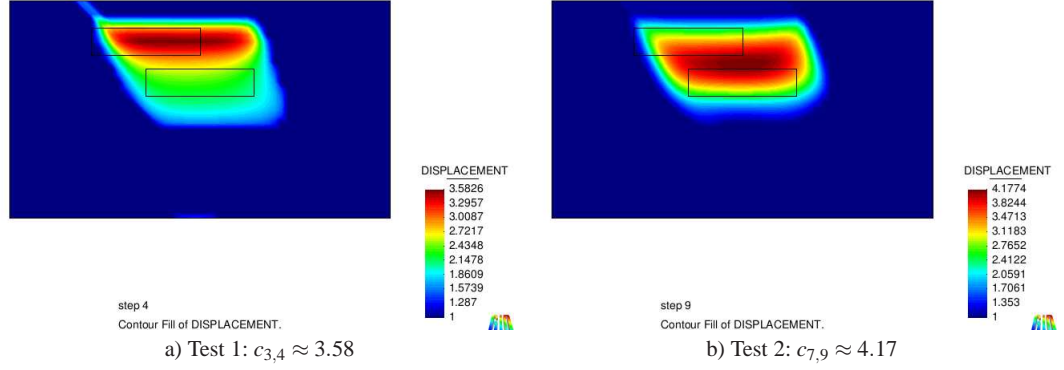


**Fig. 5** Computed image using backscattered data obtained from the geometry presented on Figure 1-a). Both location and contrast of the inclusion are accurately imaged. The computed function  $\varepsilon_r = 1$  outside of imaged inclusions. The noise level in data is 5%.

where function  $\psi_{1n}(\mathbf{x})$  and  $\psi_{2n}(\mathbf{x})$  are generated by functions  $g_0(\mathbf{x}, t)$  and  $r_0(\mathbf{x}, t)$ , respectively, see definition of IPB2. In this test we simulated the function  $r_0(\mathbf{x}, t)$  at  $I_2 \cup I_3$  by solution of the forward problem (51) with  $\varepsilon_r(\mathbf{x}) = 1$  at every point of the computational domain  $\Omega$ . This Dirichlet boundary condition at  $I_2 \cup I_3$  is also approximated and is necessary to solve the integral-differential equation (41).

As in the first test, the algorithm of section 2.5 was used to calculate the image of Figure 5-b). Location of both the mine-like targets is imaged accurately. We reconstructed contrast  $\max[\varepsilon_{r,comp}(\mathbf{x})] = 4.17$ . Thus, (49) is approximately fulfilled with 4% error of the correct value. We also note, that in this test we imaged more accurately contrast inside inclusions than in the previous test. We can conclude that in the case of backscattered data for the solution of (41) is efficient and stable apply Dirichlet boundary conditions which are immersed into data from the homogeneous domain.

### Acknowledgments

The research of the authors was supported by US Army Research Laboratory and US Army Research Office grant W911NF-11-1-0399, the Swedish Research Council, the Swedish Foundation for Strategic Research (SSF) in Gothenburg Mathematical Modelling Centre (GMMC) and by the Swedish Institute, Visby Program.

### References

1. N.V. Alexeenko, V.A. Burov and O.D. Romyantseva, Solution of three-dimensional acoustical inverse problem: II. Modified Novikov algorithm, *Acoust. Phys.*, 54, 407-419, 2008.
2. H. Ammari, E. Iakovleva, G. Perruson and D. Lesselier, Music-type electromagnetic imaging of a collection of small three dimensional inclusions, *SIAM J. Sci.Comp.*, 29, 674-709, 2007.

3. M. Asadzadeh and L. Beilina, *A posteriori* error analysis in a globally convergent numerical method for a hyperbolic coefficient inverse problem, *Inverse Problems*, 26, 115007, 2010.
4. L. Beilina and M.V. Klibanov, A globally convergent numerical method for a coefficient inverse problem, *SIAM J. Sci. Comp.*, 31, 478-509, 2008.
5. L. Beilina and M.V. Klibanov, Synthesis of global convergence and adaptivity for a hyperbolic coefficient inverse problem in 3D, *J. Inverse and Ill-posed Problems*, 18, 85-132, 2010.
6. L. Beilina and M.V. Klibanov, *A posteriori* error estimates for the adaptivity technique for the Tikhonov functional and global convergence for a coefficient inverse problem, *Inverse Problems*, 26, 045012, 2010.
7. L. Beilina, M.V. Klibanov and A. Kuzhuget, New *a posteriori* error estimates for adaptivity technique and global convergence for a hyperbolic coefficient inverse problem, *Journal of Mathematical Sciences*, 172, 449-476, 2011.
8. L. Beilina and M.V. Klibanov, Reconstruction of dielectrics from experimental data via a hybrid globally convergent/adaptive inverse algorithm, *Inverse Problems*, 26, 125009, 2010.
9. L. Beilina and M.V. Klibanov, *Approximate global convergence and adaptivity for Coefficient Inverse Problems*, Springer, New-York, 2012.
10. L. Beilina, K. Samuelsson and K. Åhlander, Efficiency of a hybrid method for the wave equation. In *International Conference on Finite Element Methods*, Gakuto International Series Mathematical Sciences and Applications. Gakkotosho CO., LTD, 2001.
11. V.A. Burov, S.A. Morozov and O.D. Rummyantseva, Reconstruction of fine-scale structure of acoustical scatterers on large-scale contrast background, *Acoustical Imaging*, 26, 231-238, 2002.
12. K. Chadan and P.C. Sabatier, *Inverse Problems in Quantum Scattering Theory*, Springer-Verlag, New York, 1989.
13. Y. Chen, R. Duan and V. Rokhlin, On the inverse scattering problem in the acoustic environment. *J. Comput. Phys.*, 228, 3209-3231, 2009.
14. M. Cheney and D. Isaacson, Inverse problems for a perturbed dissipative half-space, *Inverse Problems*, 11, 865- 888, 1995.
15. D. Isaacson, J.L. Mueller, J.C. Newell and S. Siltanen, Imaging cardiac activity by the D-bar methods for electrical impedance tomography, *Physiological Measurements*, 27, S43-S50, 2006.
16. M. V. Klibanov, Uniqueness of solutions in the 'large' of some multidimensional inverse problems, in *Non-Classical Problems of Mathematical Physics*, 101–114, 1981, published by Computing Center of the Siberian Branch of the USSR Academy of Science, Novosibirsk (in Russian).
17. M. V. Klibanov and A. Timonov, A unified framework for constructing the globally convergent algorithms for multidimensional coefficient inverse problems, *Applicable Analysis*, 83, 933-955, 2004.
18. M. V. Klibanov and A. Timonov, *Carleman Estimates for Coefficient Inverse Problems and Numerical Applications*, VSP, Utrecht, 2004.
19. M. V. Klibanov, M. A. Fiddy, L. Beilina, N. Pantong and J. Schenk, Picosecond scale experimental verification of a globally convergent numerical method for a coefficient inverse problem, *Inverse Problems*, 26, 045003, 2010.
20. M.V. Klibanov, J. Su, N. Pantong, H. Shan and H. Liu, A globally convergent numerical method for an inverse elliptic problem of optical tomography, *Applicable Analysis*, 6, 861-891, 2010.
21. A. V. Kuzhuget and M. V. Klibanov, Global convergence for a 1-D inverse problem with application to imaging of land mines, *Applicable Analysis*, 89, 125-157, 2010.
22. A.V. Kuzhuget, N. Pantong and M.V. Klibanov, A globally convergent numerical method for a coefficient inverse problem with backscattering data, *Methods and Applications of Analysis*, 18, 47-68, 2011.
23. R.G. Novikov, The  $\partial$ -bar approach to approximate inverse scattering at fixed energy in three dimensions, *Int. Math. Res. Reports*, 6, 287-349, 2005.

24. L. Pestov, V. Bolgova, O. Kazarina, Numerical recovering of a density by the BC-method. *Inverse Probl. Imaging*, 4, 703-712, 2010.
25. Portable, Extensible Toolkit for Scientific Computation PETSc at <http://www.mcs.anl.gov/petsc/>
26. V.G. Romanov 1986 *Inverse Problems of Mathematical Physics* (Utrecht, The Netherlands: VNU).
27. Tables of dielectric constants at <http://www.asiinstr.com/technical/DielectricConstants.htm>.
28. J. Xin and M. V. Klibanov, Numerical solution of an inverse problem of imaging of antipersonnel land mines by the globally convergent convexification algorithm, *SIAM J. Sci. Comp.*, 30, 3170-3196, 2008.
29. Software package WavES at <http://www.waves24.com/>